Trial Version Wondershare PDFelement

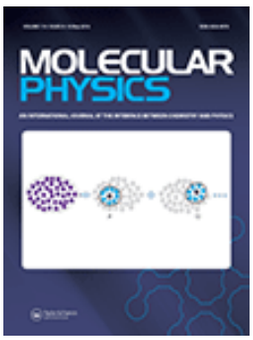

**Molecular Physics**

An International Journal at the Interface Between Chemistry and Physics

ISSN: (Print) (Online) Journal homepage: https://www.tandfonline.com/loi/tmph20

# Excited state dynamics in a sodium and iodine co-doped lead telluride nanowire

**Kevin Gima , Talgat M. Inerbaev & D. S. Kilin**

**To cite this article:** Kevin Gima , Talgat M. Inerbaev & D. S. Kilin (2021): Excited state dynamics in a sodium and iodine co-doped lead telluride nanowire, Molecular Physics, DOI: 10.1080/00268976.2021.1874557

**To link to this article:** https://doi.org/10.1080/00268976.2021.1874557

View supplementary material

Published online: 22 Jan 2021.

Submit your article to this journal

View related articles

View Crossmark data

Full Terms & Conditions of access and use can be found at
https://www.tandfonline.com/action/journalInformation?journalCode=tmph20

Trial Version Wondershare PDFelement

MOLECULAR PHYSICS e1874557
https://doi.org/10.1080/00268976.2021.1874557

Taylor & Francis
Taylor & Francis Group

60TH SANIBEL SYMPOSIUM

Check for updates

# Excited state dynamics in a sodium and iodine co-doped lead telluride nanowire

Kevin Gima[a], Talgat M. Inerbaev [b,c,d] and D. S. Kilin [e]

[a]Department of Physics, North Dakota State University, Fargo, ND, USA; [b] L. N. Gumilyov Eurasian National University, Nur-Sultan, Kazakhstan; [c]Sobolev Institute of Geology and Mineralogy SB RAS, Novosibirsk, Russia; [d]National University of Science and Technology MISIS, Moscow, Russian Federation; [e]Department of Chemistry and Biochemistry, North Dakota State University, Fargo, ND, USA

**ABSTRACT**

Materials that convert wasted heat into electricity are needed to help solve global warming and other climate challenges. Thermoelectric nanowires are novel metamaterials for such applications. Non-adiabatic coupling computations are critical in understanding thermally activated charge transfer in thermoelectric materials. Here, non-adiabatic computations are used to evaluate electron relaxation rates in lead telluride nanowires. This work reports results on PbTe (lead telluride) atomistic models doped with sodium and iodine that contain 288 atoms in simulation cells with periodic boundary conditions. The calculations are performed on the basis of ground-state DFT under the VASP software. The transitions between states are modelled in terms of Redfield equation of motion parameterised by on-the-fly non-adiabatic couplings along thermalised molecular dynamic trajectory. The initial states are approximated by the promotion of an electron from occupied to unoccupied Kohn–Sham orbital. In each transition, the change of the energy and spatial charge distribution with respect to time were calculated, demonstrating formation of charge transfer. The trends of electron and hole relaxation rates comply with the energy gap law.

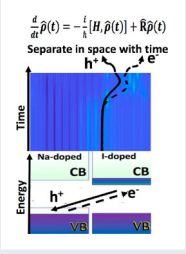


**ARTICLE HISTORY**
Received 30 April 2020
Accepted 6 January 2021

**KEYWORDS**
Lead telluride; density matrix; charge transfer; co-doping; non-adiabatic

## Introduction

Semiconductors are utilised in modern technologies for cellphones, refrigerators, automobiles, microwaves and numerous other ones. Applying thermoelectric materials to semiconductors can convert their excess waste heat into electricity, thus improving their efficiency. Thermoelectric materials use a temperature gradient between heat source and heat sink to produce a current. The phenomenon, where an electric potential (Voltage) is produced in a thermoelectric material placed between heat source and heat sink, is known as the Seebeck effect. This effect is measured by a material's figure of merit given by $zT = ((\sigma S^2 T)/\kappa)$ where S is the Seebeck coefficient, $\kappa$ thermal conductivity, $\sigma$ electrical conductivity, and T temperature [1]. One aims to maximise this parameter. Oftentimes one achieves such improvements by doping (adding impurities) various materials [2]. In case the free charges are positive (the material is p-type), positive charge will build up near the heat sink (on the cold end) which will have a positive potential. Similarly, negative free charges (n-type material) will produce a negative potential near the heat sink (at the cold end). See SI for details.

Lead telluride is considered a promising thermoelectric material due to the reported high figure of merit. Heremans *et al.* achieved a figure of merit of 1.5 at 773 K with a thallium-doped lead telluride [3]. Snyder *et al.* obtained a 1.4 figure of merit at 750 K with a

**CONTACT** D. S. Kilin dmitri.kilin@ndsu.edu

Supplemental data for this article can be accessed here. https://doi.org/10.1080/00268976.2021.1874557

© 2021 Informa UK Limited, trading as Taylor & Francis Group

Trial Version Wondershare PDFelement

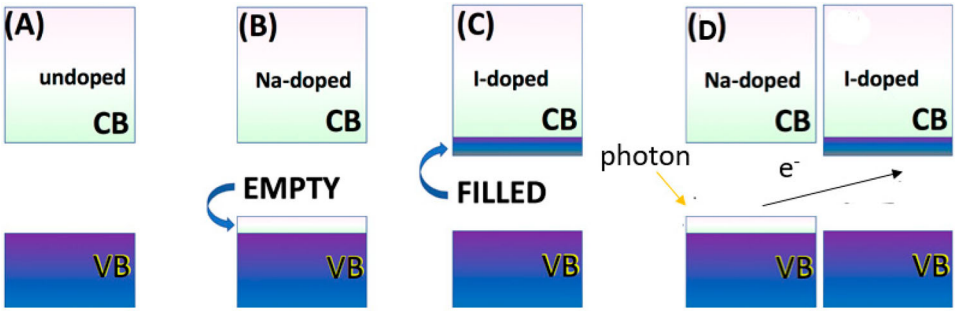


**Figure 1.** Electronic structures of various doped and un-doped nanowires (A) In the un-doped state, both valence and conduction bands are unchanged (B) In Na-doped state, one electron is taken from the valence band. (C) In the I-doped state, a hole from the conduction band is removed. In other words, this hole is filled with an electron. (D) This combines both Na and I doping. Charge transfer of an electron upon photo-excitation from sodium's valence band to sodium's conduction band is illustrated.

sodium-doped lead telluride [4], and a 1.8 figure of merit at 850 K with a sodium-doped $PbTe_{1-x}Se_x$ alloy [5]. Also, a different group of researchers produced a figure of merit of 2.2 with the material [6,7]. See Figure 1 for a schematic diagram of sodium and iodine doping, which are typical implementations of p- and n- doping for lead telluride.

The basis for computational and theoretical chemistry is the time-dependent molecular Schrödinger equation (see details in SI). Since the ions' mass is much greater than electrons', the molecular Schrödinger equation is solved by separating the equation into an electronic and ionic part. These equations are then solved by using one of the established methods. Examples include Hartree–Fock, CI Coupled Cluster, or the density functional theory (DFT) method in order to calculate electronic properties. Although DFT is accurate enough for the ground-state properties, one finds that more advanced and computationally extensive methods are needed for excited state dynamics and analysis.

This complex modelling helps researchers obtain more accurate predictions of excitation states' properties. The two types of excitations are optical and thermal. Photons induce optical excitations that change the electronic state. Thermal excitations by phonons change the motion of ions' position and change population of states near the bandgap. Thermalised molecular dynamics models the motion of atoms along with their change in energy with time. The motion of the atoms is defined by Newton's equation of motion and the potential energy and force are incorporated using force fields or recomputed at each step via electronic structure methods and using Hellman-Feynman Theorem.

An important challenge is assessing changes in electronic degrees of freedom induced by interaction with nuclear degree of freedom. The explicit monitoring of both electronic and nuclear degrees of freedom is often forbidden by high computational cost. There is a popular way to address this challenge by using the so-called open quantum system approach, where the primary system of interest experiences influence of environment in the thermal equilibrium. Often, the primary system is represented by electronic degrees of freedom and environment in thermal equilibrium is represented by nuclear degrees of freedom. This approach extends the concept of density operator from static domain to dynamic domain.

Density operator characterises quantum state of the system and is a more general concept than the wave function. In case density operator is available, one can use it for calculating expectation value for any operator representing an observable, by the trace operation: $A = Tr(\hat{\rho}_{tot}\hat{A})$. The density operator of the complete system can be converted into reduced density operator of the electronic degrees of freedom, by performing an averaging procedure over all nuclear degrees of freedom, which are assumed to reside in thermal equilibrium. Most interesting and useful is the application of the density operator concept to situations when the primary system is prepared in the non-equilibrium states and performs time evolution towards the equilibrium. There are several practical implementations for describing such dynamic such as the Redfield equation [8,9]. The Born-Oppenheimer approximation is of limited applicability to important processes such as charge transfer and relaxation in one-dimensional lead telluride nanowires, which is due to the energy flow between the electronic part and nuclear part [10,11]. The electronic relaxation process based on surface hopping between potential energy surfaces was successfully completed by several groups [12]. Various methods, ranging from density functional theory [13–15] to high-precision non-adiabatic excited state molecular dynamics [16–19], have been utilised to model this process in other structures. The feasibility of molecular dynamic trajectory for computing

Trial Version Wondershare PDFelement

the electron-to-lattice coupling in semiconductors seems very efficient [20,21]. The integration of TDDFT and molecular dynamic methods was recently proved to be an efficient approach [22,23].

According to Egorova *et al.* [24], multilevel Redfield theory is a useful approach for electronic relaxation. This theory is efficient in the limits of the dynamics that occurs on extended time intervals, low couplings, and multiple electronic states [8,24–31]. This theory is further supported by a compromise between precision and practical efficiency. The balance between the following benefits, shortcomings, and features of Redfield theory is considered while selecting a method for this work: (i) Redfield theory is a specific application of the density matrix equation of motion and, therefore it predicts the electronic properties of more phenomena as opposed to the wavefunction, surface hopping, or Pauli Master equation approaches: (ii) Redfield theory is easily used in tandem with ab initio computation. It is clear which parameters must be computed and used, with an efficient algorithm for computation. (iii) Redfield theory might not be the most precise, for example a method of non-equilibrium Green's function is more general and potentially precise, but much less practical [32]. There is an attempt to combine Redfield theory with electrons-to-lattice coupling to achieve on-the-fly electron and hole relaxation [33,34]. Optimum results are expected in the following conditions: ions are considered as point charges, lattice vibrations instantaneously equilibrate with a thermostat, coupling autocorrelation function decays abruptly leading to Markov approximation. In addition, we assume that the inter-nuclear forces and distances do not respond to the change in electronic state. Thus, nuclear reorganisation is neglected, and excited state potential energy surfaces are assumed to have the same shape as the ground-state potential energy surfaces.

The paper is organised as follows: The key steps of the computational protocol are sketched in the Methods section, for consistency of notation. The Results section starts with the discussion of computational model composition and later provides results on static and dynamic observables for this model. Choices of exchange–correlation functional are analysed in the Discussion section. The main findings of this work are outlined in the conclusions section.

## Methods

The electronic structure is determined by using the density functional theory (DFT) [35] implemented in the VASP software [36]. The main equation is a fictitious one-electron Kohn–Sham [37] equation

$$\left(-\frac{\hbar^2}{2m}\nabla^2 + v\left(\vec{r},[\rho(\vec{r})],\{\vec{R}_I\}\right)\right)\varphi_i^{KS}\left(\{\vec{R}_I\},\vec{r}\right) = \varepsilon_i\left(\{\vec{R}_I\}\right)\varphi_i^{KS}\left(\{\vec{R}_I\},\vec{r}\right) \quad (1)$$

where the first term corresponds to kinetic energy $T$ and uses symbol of gradient $\nabla = (\partial/\partial x, \partial/\partial y, \partial/\partial z)$. In Equation (1) we find a set of one-electron orbital's $\varphi_i^{KS}(\{\vec{R}_I\},\vec{r})$and their energies $\varepsilon_i$. The orbitals are combined with orbital occupation function $f_i$ for constructing the total density of electrons

$$\rho(\vec{r}) = \sum_i f_i \varphi_i^{KS^*}(\vec{r})\varphi_i^{KS}(\vec{r}) \quad (2)$$

Note that here the density is composed out of pairs of orbitals with coinciding indices. Total density determines the potential

$$v[\overrightarrow{r},\rho] = \delta/\delta\rho(E^{tot}[\rho] - T[\rho]) \quad (3)$$

which is defined as functional derivative of the total energy in respect to variation of the total density and includes interactions of electrons with ions, and three electron interactions: Coulomb, correlation, and exchange. Rectangular brackets symbolise functional. Equations (1)–(3) are solved in the iterative, self-consistent manner by using VASP software according to Perdew–Burke–Ernzerhof procedure (PBE-functional) [38,39] although the use of other functional is also possible. The choice of functional does affect results for the bandgaps, electronic density of states, spatial distribution of orbitals, MD trajectories, and non-adiabatic couplings. The choice of functional effect of each of these characteristics in different extent is analysed in the Discussion section.

The electron density of states (DOS) describes the number of states per interval of energy. One uses DOS to characterise electronic structures of the studied models. DOS is defined as

$$n(\varepsilon) = \sum_i \delta(\varepsilon - \varepsilon_i) \quad (4a)$$

where the Dirac delta function was approximated with a finite width Gaussian function.

One of the parameters obtained from the DFT calculation is the *oscillator strength* representing probability that a model, which absorbs a photon, will undergo an electronic transition. Thus, the oscillator strength is related to the rate of absorption and is defined as

$$f_{ij} = \frac{4\pi m_e \omega_{ij}}{3he^2}|\vec{D}_{ij}|^2 \quad (4b)$$

where $\omega_{ij} = ((\varepsilon_i - \varepsilon_j)/\hbar)$ is the angular frequency required to excite an electron from state $i$ to state $j$. $\vec{D}_{ij} =$

Trial Version Wondershare PDFelement

$e\int d\vec{r}\varphi_i^*(\vec{r})\cdot\vec{r}\cdot\varphi_j(\vec{r})$ is the transition dipole moment for transition from state $i$ to state $j$, and $m_e$, $h$, and $e$ are fundamental constants. The spectral density of absorption was calculated analogously to the DOS using

$$\alpha(\omega)=\sum_{i\le HO}\sum_{j\ge LU} f_{ij}\delta(\hbar\omega-\hbar\omega_{ij}) \tag{5a}$$

Here, two sums run over *pairs of orbitals*. Each delta function is weighted by the oscillator strength corresponding to the transition, so that the more probable transitions are given a greater weight in the total absorption spectrum. Delta function is approximated by the finite width function with width parameter corresponding to a spectral line broadening due to the Heisenberg uncertainty principle and thermal fluctuations.

The orbitals computed by Equation (1) are visualised and interpreted in the form of 3D iso-surfaces of partial charge density, for selected orbital $|\varphi_i^{KS}(\vec{r})|^2$ or by 1D distributions

$$\rho_i(z)=\iint dxdy|\varphi_i^{KS}(x,y,z)|^2 \tag{5b}$$

The main goal of this work is to explore non-equilibrium dynamics of electronic state of the models of interest. There are two important factors that determine non-equilibrium dynamics: initial excitation and non-radiative relaxation originating from interaction between electronic and nuclear degrees of freedom. Generally, one can assess interaction of electronic and nuclear degrees of freedom based on the response of electronic system to elongation of nuclear degrees of freedom along normal mode coordinates. Such approach is often used for solids at low temperatures when the nuclear motion is described as harmonic oscillations near equilibrium. However, at elevated temperatures, in the non-harmonic regime, one often uses the so-called 'on-the-fly' evaluation, which is computed along nuclear trajectories. This approach was developed by researchers such as John Tully, David Micha, Sharon Hammes-Schiffer, Oleg Prezhdo, Sergei Tretiak, Hans Lishka, and others. In order to implement this approach, one first needs to review basics of the computation of first principles molecular dynamics trajectory which is accomplished in two stages: *heating* and actual *molecular dynamics*.

*Heating*. The heating algorithm then reheats or cools the system depending on if the average atoms' momenta are higher or lower for the specific temperature. After initial calculations using DFT and VASP software, the system is then heated to a specific temperature which increases its kinetic energy.

$$\sum_{I=1}^{N}\frac{M_I\left(\frac{d\vec{R}_I}{dt}|_{t=0}\right)^2}{2}=\sum_{I=1}^{N}\frac{(\vec{P}_I)^2}{2M_I}=\frac{3}{2}Nk_BT \tag{6}$$

The system is then allowed to move for an infinitesimal amount of time to redistribute between kinetic and potential energy domains. This procedure is repeated several times until kinetic energy stabilises near the requested value. The heating step provides initial conditions for the next step, for the molecular dynamics. The positions $\{\vec{R}_I(t)\}$ and momenta $\{\vec{P}_I(t)\}$ at the last steps of the heating stage are used as input parameters, as initial conditions for the molecular dynamic stage.

*Molecular dynamics*. After the heating step, the molecular dynamics step begins.

$$\frac{d^2\vec{R}_I(t)}{dt^2}=\frac{1}{M_I}\vec{F}_I(t) \tag{7}$$

Here, the trajectory of each ion $\vec{R}_I(t)$ is obtained by integrating Newton's equation motion with initial conditions originating from the heating stage. Note that, in the *ab initio* molecular dynamics, the Force $\vec{F}_I(t)$ is recomputed at each time step, based on electronic structure data, as an observable, using Hellman Feynman theorem.

After obtaining trajectories of position of ions and set of Kohn-Sham orbitals at each step of the trajectory using first principles molecular dynamics, non-adiabatic couplings were computed. The non-adiabatic coupling is the tool to assess the interaction between electronic and nuclear degrees of freedom. The non-adiabatic coupling is the measure of maintaining or violating of the orthogonality between two orbitals.

$$\begin{aligned}V_{ij}(t)&=-i\hbar<\psi_i^{KS}\{\vec{r},\vec{R}_I(\mathrm{t})\}|\frac{d}{dt}|\varphi_j^{KS}\{\vec{r},\vec{R}_I(t)\}\rangle\\&=\frac{-i\hbar}{2\Delta t}\iiint d\vec{r}(\varphi_i^{KS*}\{\vec{r},\vec{R}_I(\mathrm{t}+\Delta t)\}\\&\quad\times\varphi_j^{KS}\{\vec{r},\vec{R}_I(\mathrm{t})\}+\psi_i^{KS*}\{\vec{r},\vec{R}_I(\mathrm{t})\}\\&\quad\times\varphi_j^{KS}\{\vec{r},\vec{R}_I(\mathrm{t}+\Delta t)\})\end{aligned} \tag{8}$$

In Equation (11) we find how the orthogonality of two orbitals, $\varphi_i^{KS}(\{\vec{R}_I\},\vec{r})$ and $\varphi_j^{KS}(\{\vec{R}_I\},\vec{r})$ is kept or violated if the orbitals are evaluated at nearby steps of the nuclear trajectory, offset by time step $\Delta t$. One computes the coupling $V_{ij}(t)$ for all available pair of the orbitals. The value of such coupling for a provided pair of orbitals does experience fast oscillations, and needs two things: (A) to be averaged and (B) to be transferred from time domain to frequency domain, as described in what follows:

(A) The averaging procedure is performed in terms of the autocorrelation function computed for two pairs of orbitals $V_{ij}^{NA}(t+\tau)$ and $V_{kl}^{NA}(t)$ evaluated at different times.

$$M_{ijkl}(\tau)=\frac{1}{T}\int_0^T V_{ij}^{NA}(t+\tau)V_{kl}^{NA}(t)dt \tag{9a}$$

Trial Version Wondershare PDFelement

This autocorrelation function uses an average over the time interval $T$, which is the duration of the whole trajectory. In addition, thee autocorrelation function is related to the transition rate between orbitals. Also, note that most important elements of the autocorrelation are those with coinciding pairs of indices $M_{ijij}$, which deal with population relaxation. Other values do correspond to de-coherence.

(B) The Fourier transform of $M_{ijkl}$(t) is often referred to and Redfield tensor and is denoted as $R_{ijkl}$.

$$R_{ijkl} = \Gamma^{+}_{ljik} + \Gamma^{-}_{ljik} - \delta_{lj}\sum_{m}\Gamma^{+}_{immk} - \delta_{ik}\sum_{m}\Gamma^{-}_{lmmj}, \tag{9b}$$

$$\Gamma^{+}_{ijkl} = \int d\tau M_{ijkl}(\tau) exp(-i\omega_{kl}\tau), \tag{9c}$$

$$\Gamma^{-}_{ijkl} = \int d\tau M_{ijkl}(\tau) exp(-i\omega_{ij}\tau), \tag{9d}$$

The details on the computation of this tensor are available in the original paper by A.G. Redfield and a range of papers on non-equilibrium dynamics.

The elements of the Redfield tensor have an analogy to Fermi's golden rule. A transition from instantaneous non-adiabatic coupling to the rates averaged over trajectory corresponds to Markoff approximation and allows formulating differential equation of motion for density operator without memory kernel.

After calculating this transition rates, reduced density matrix dynamics is used to find how the density operator changes with time. Equation of motion for density matrix includes Liouvillian $-(i/\hbar)[H, \hat{\rho}(t)]$ and Redfield $\hat{\mathrm{R}}\hat{\rho}(t)$ terms.

$$\frac{d}{dt}\hat{\rho}(t) = -\frac{i}{\hbar}[H, \hat{\rho}(t)] + \hat{\mathrm{R}}\hat{\rho}(t) \tag{10a}$$

After plugin in the definition of density $\rho(\vec{r}) = \sum_{ij}\rho_{ij}\varphi_j^{KS^*}(\vec{r})\varphi_i^{KS}(\vec{r})$ into Equation (10a) one obtains the equation in terms of density matrix and matrix elements.

$$\frac{d}{dt}\rho_{ij}(t) = -\frac{i}{\hbar}\sum_{k}(H_{ik}\rho_{kj} - \rho_{ik}H_{kj}) + \sum_{kl}\mathrm{R}_{\mathrm{ijkl}}\rho_{kl}(t) \tag{10b}$$

Note that the density considered here is time dependent. It contrasts the ground-state density in the original density functional theory, which is time-independent. It is interesting to discuss similarities and differences between equation of motion for density matrix (10b) and kinetic Boltzman equation introduced in e.g. Ref. [40]. The Redfield term of (10b) would correspond to scattering term in Boltzman equation, while Liouvillian term of (10b) approximately relates to diffusive and filed-related terms of Boltzman equation. For an adequate comparison, both equations must be compared in either time-dependent form or for the stationary state, when $(d/dt)\rho_{ij}(t) = 0$. Also, for the complete analogy, to introduce a concept of local temperature for both Boltzman and Redfield equations. After the density matrix dynamics trajectory $\rho_{ij}(t)$ is calculated, one can move to the task of computing observables. Note that the diagonal elements of density matrix $\rho_{ii}$ correspond to the population of orbital $i$.

Another important aspect is that features of the dynamics depend on the initial condition

$$\rho_{ij}(0) = \rho_{ij}(\infty) - \delta_{ia} + \delta_{jb} \tag{10c}$$

defined here as an electron promoted from the occupied orbital $a$ to the unoccupied orbital $b$.

## Observables

The overall picture of charge density evolution in time can be analysed in the form of mapping solution for density matrix into distribution as function of energy

$$\Delta n(\varepsilon, t) = \sum_{i}(\rho_{ii}(t) - \rho_{ii}(\infty))\delta(\varepsilon - \varepsilon_i) \tag{11}$$

The expectation value of electron and hole energy is calculated using

$$\langle E_e\rangle(t) = \sum_{i\geq LU}\rho_{ii}(t)\varepsilon_i(t) \tag{12a}$$

$$\langle E_h\rangle(t) = \sum_{i\leq HO}\rho_{ii}(t)\varepsilon_i(t) \tag{12b}$$

Note that $\sum_{i\leq HO}\rho_{ii} = \sum_{i\geq LU}\rho_{ii} = 1$. Interestingly, for excitations defined in Equation (10c) at $t = 0$ expectation energy of the charge carrier is equal to the energy of excited orbital $\langle E_e\rangle(\mathrm{t}=0) = \varepsilon_{\mathrm{i=b}}$; $\langle E_h\rangle(\mathrm{t}=0) = \varepsilon_{\mathrm{j=a}}$. Finally, the rate of relaxation is calculated using either one of the following equations:

$$k_{e/h} = \frac{dE_{e/h}(t)}{dt} \tag{13}$$

$$k_{e/h} = \{\tau^{e/h}\}^{-1} = \left\{\int_0^{\infty} E_{e/h}(t)dt\right\}^{-1} \tag{14}$$

The main goal of this study is to determine if the relaxation rates follow the band gap law as follows:

$$k_{e/h} = Ae^{-\alpha\Delta\mathrm{E}};\quad \ln k_{e/h} - \ln A = -\alpha\Delta\mathrm{E} \tag{15}$$

Also, it is important to note that charge density evolution in time can be analysed in the form of mapping solution for density matrix into a charge density distribution

Trial Version Wondershare PDFelement

as a function of position in space

$$\Delta n^e(z,t) = \sum_{i \geq LU} (\rho_{ii}(t) - \rho_{ii}(\infty))\rho_i(z) \tag{16a}$$

$$\Delta n^h(z,t) = \sum_{i \leq HO} (\rho_{ii}(t) - \rho_{ii}(\infty))\rho_i(z) \tag{16b}$$

$$\Delta n(z,t) = \Delta n^e(z,t) - \Delta n^h(z,t) \tag{16c}$$

Here $\rho_i(z)$is defined in Equation (5b). The distributions $\Delta n(z,t)$ serve as a complementary tool for the analysis of solution for density matrix and, they also may help in establishing similarities and differences between density-matrix approach and Boltzmann equation, as discussed in Ref. [40]. The distributions $\Delta n(z,t)$ allow tracking expected spatial position of negative $\langle z_e \rangle(t)$ and positive $\langle z_h \rangle(t)$ charge carriers.

$$\langle z_e \rangle(t) = \int z \Delta n^e(z,t) dz \tag{16d}$$

$$\langle z_h \rangle(t) = \int z \Delta n^h(z,t) dz \tag{16e}$$

The spatial separation of positive and negative charge carriers

$$\langle d \rangle(t) = \langle z_h \rangle(t) - \langle z_e \rangle(t) \tag{16f}$$

is related to the electric field and voltage at the interface, as shown in Refs. [41–43]. It is interesting to discuss differences and similarities of voltage in the same interface, originating from a photoinduced charge separation and voltage created by a temperature gradient $E = Q\, grad\, T$, as introduced in Equation (59) in Ref. [44].

## Results

In this study, a periodic lead telluride nanowire, doped with sodium and iodine (Figure 2), was examined. The nanowire is surrounded by 1nm of vacuum in x- and y- directions, separating it from the periodic images. The simulation cell length is 110 angstroms along z-direction and possesses a cubic structure with 288 atoms. Lead and telluride occur in a 1:1 ratio, with two iodine and sodium atoms. Lead donates its two excess electrons to telluride, so it can complete its valence shell. This is illustrated in the following equation:

$$Pb^{2+} + Te^{2-} = PbTe \tag{17}$$

This work is based on understanding of the charge balancing of dopants in the doping process. Doping is the process of inserting impurities into a semiconductor to modify its properties. For instance, sodium doping works as follows:

$$\begin{aligned}[Na^{(0)} \rightarrow Na^{(1+)} + 1e^-] - [Pb^{(0)} \rightarrow Pb^{(2+)} + 2e^-] \\ = Na^{(0)} - Pb^{(0)} \rightarrow 1e^- - 2e^- = -1e\end{aligned} \tag{18}$$

In Equation (18), sodium has one extra electron in its valence band. In contrast, lead has two extra electrons. When sodium replaces lead in the doping process, one electron is displaced from the valence band.

$$\begin{aligned}[I^{(0)} \rightarrow I^{(1-)} - 1e^-] - [Te^{(0)} \rightarrow Te^{(2-)} - 2e^-] \\ = I^{(0)} - Te^{(0)} \rightarrow -1e^- - (-2e^-) = 1e^-\end{aligned} \tag{19}$$

In Equation (19), iodine has a hole in its valence shell. As previously stated, telluride has two holes in its shell. In iodine doping, the iodine replaces the telluride. After doping, one hole is removed from the conduction band, which is equivalent to adding an electon to the conduction band.

Figure 3 shows density of states for the un-doped and co-doped PbTe NW, computed according to Equation 4(a). Figure 3(a) shows an un-doped lead telluride rectangular nanowire. The computed bandgap here is approximately 1 eV. In the conduction band, the numerous orbitals with energies ranging from 1.5 to 2 eV provode larger density of states. This is compared to Figure 3(b) for the co-doped nanowire. In the valence band, in the range from −2 eV to 0 eV there is the larger number of states available. Note the purple colour indicates that these states are occupied by electrons. Note that a larger number of states are available for the doped model. Furthermore, the bandgap here has slightly decreased to 0.9 eV. These two changes indicate a drastic increase in the co-doped nanowire's ability to facilitate charge transfer.

Unoccupied conduction band peaks B,D in Figure 3(a) correspond to unoccupied conduction band peaks b, d in

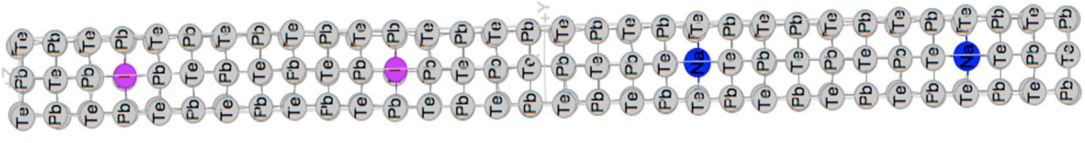

**Figure 2.** A rectangular PbTe nanowire doped with iodine (pink) and sodium (blue). The original, undoped model of the nanowire is composed of 16 pairs of alternating layers $Pb_5Te_4$ and $Pb_4Te_5$, yielding composition $Pb_{144}Te_{144}$. In the doped model, sodium replaces lead atoms due to excess electrons in their valence band. Conversely, iodine replaces telluride due to excess holes in their conduction band, yielding composition $Pb_{142}Na_2Te_{142}I_2$. This study examines if this doping configuration improves charge transfer.

Trial Version Wondershare PDFelement

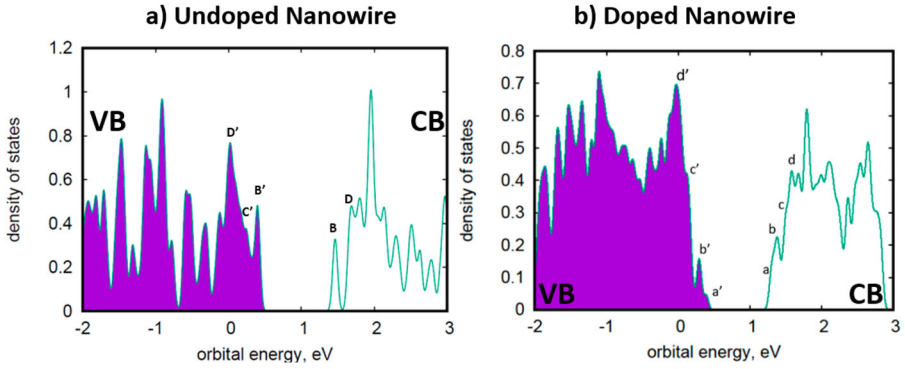


**Figure 3.** Density of States. Note that the filled area for doped nanowire is greater than un-doped, indicating a greater number of states. Furthermore, the doping process added extra states a and c in the conduction band and a′ in the valence band. a and a′ are congruent with the extra states added to both bands in Figure 1(d).

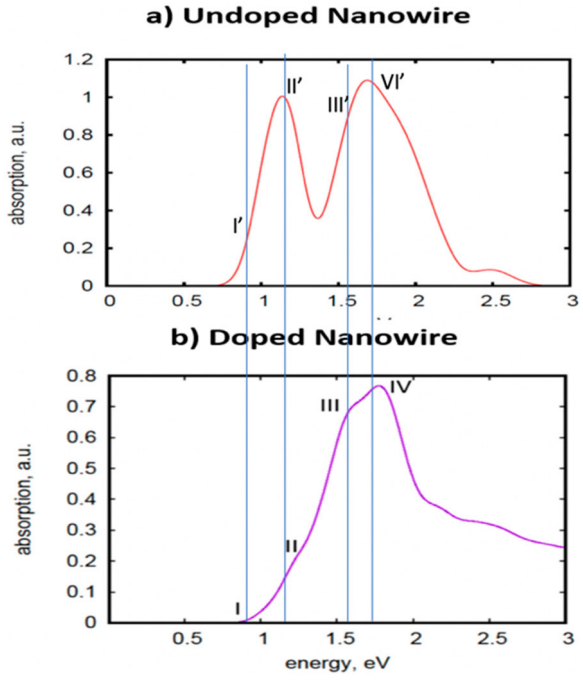


**Figure 4.** Absorption spectra (a) un-doped and (b) doped nanowires. In (a), the lowest transition is bright due to non-overlap between B and B′ in Figure 6(a). In contrast, lowest transition in (b) is dark due to charge transfer excitation.

Figure 3(b). Peaks a, c in the co-doped model are unique and do not have counterparts as they are contributed by iodine. Occupied peaks B', C', D' in the valence band of Figure 3(a) correspond to occupied peaks b', c', d' in valence band of Figure 3(b). The occupied peak a' in co-doped VB does not have analogues as it is contributed by sodium. So, it can be concluded from the analysis of DOS that the frontier orbitals of the co-doped model are contributed by dopants and the lowest excitation is expected to have the charge transfer character.

Figure 4 presents absorption spectra of the un-doped and co-doped models, computed by Equation (5). Overall intensity of absorption is higher for un-doped than for the co-doped model. In notations of Figure 3(a), the transition from B' to B is expected to be bright due to their delocalisation over telluride and lead ions, respectively. Thus, these states will have significant overlap and therefore increased value of oscillator strength.One expects that transitions between orbitals of the similar symmetry (b' to b) are available in the doped nanowire and contribute intense features to absorption spectrum.

Additionally, in Figure 4(b), the absorption spectra of the doped nanowire are shown in comparison with the un-doped nanowire. Note that the lowest transition (I) in Figure 4(b) corresponds to transition from a' to a in Figure 3(b) and is dark due to charge transfer excitation. This is congruent with the expected results since the electron is experiencing a transition between orbitals with different spatial localisation, and negligible overlap, that disables the intensity of optical transition. Note that features a' and a in Figure 3(b) correspond to orbitals localised near the sodium and iodine dopants, respectively. In short, spectral features shown in Figure 4(a) and Figure 4(b) differ due to the dopants-contributed states a and a' in the DOS of the doped model.

Figure 5 shows some representative orbitals that were considered in the study. The most important trend to note here is orbital localisation. In other words, all the occupied orbitals are found near the sodium dopants, and the unoccupied orbitals are near the iodine dopants. This is consistent with the chemical structure of both iodine and sodium. The best example for this is in Figure 5(d) which illustrates the HOMO. In this case, it is clearly shown that all occupied orbitals are localised in the part of the nanowire doped by sodium. Likewise, all the unoccupied orbitals are localized near the part of the nanowire doped by iodine.

Figure 6 illustrates 1D distributions of Kohn–Sham orbitals computed by Equation 5(b). Figure 6 further supports Figure 5. This shows that the orbitals of the conduction and valence bands are in the vicinity of the

Trial Version Wondershare PDFelement

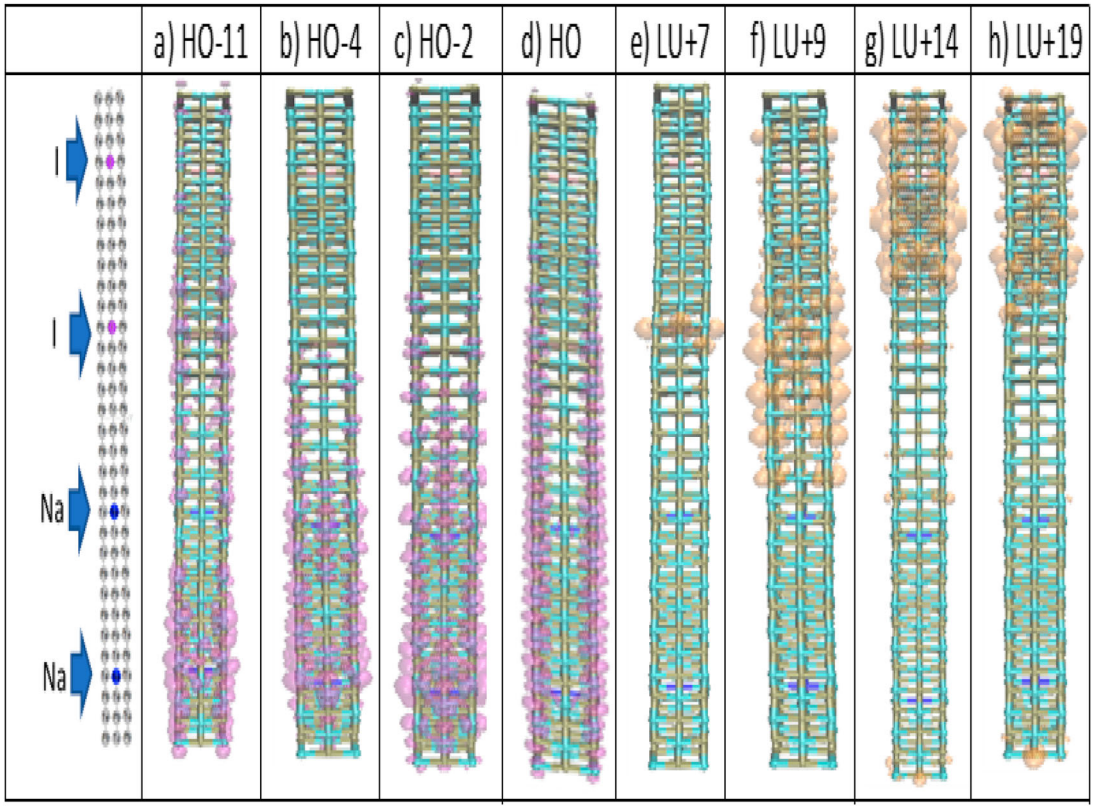


**Figure 5.** Kohn-Sham Orbitals' localisation. This figure shows all orbitals that were considered in this study. Note that all HO orbitals are localised near the sodium dopants. Conversely, all LU orbitals are localised around the iodine dopants.

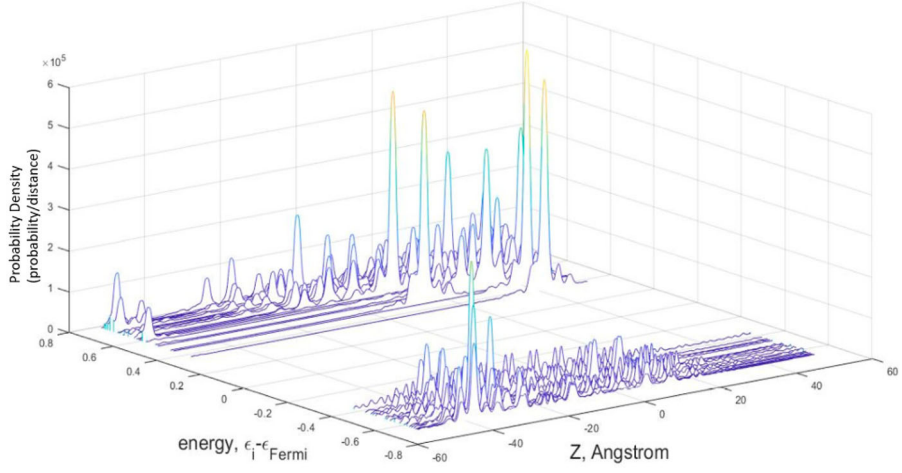


**Figure 6.** Probability density as a function of atomic distance and orbital energy. Congruent with Figure 5, the conduction and valence bands are localised around the sodium ($z < 0$) and iodine ($z > 0$) dopants. Note that probability appears highest at the conduction band (0–60 Angstroms).

I and Na dopants, respectively, in agreement with the preceding figure. Also, theabsolute values of density for the unoccupied orbitals are higher. Unoccupied orbitals are localized in the close vicinity of I -dopants, while occupied orbitals are delocalized over the whole space region doped by Na.This is expected since the electron is travelling to fill the hole in iodine.

Kohn–Sham orbital energies are fluctuating along molecular dynamics trajectory. It is very interesting to discuss how the band gap changes with time. Since $\vec{R}_I = \vec{R}_I(t)$ and $\varepsilon_i = \varepsilon_i(R)$, this implies that $\varepsilon_i = \varepsilon_i\left(\{\vec{R}_I\}(t)\right)$ where $\vec{R}_I$ and $\varepsilon_i$ stand for the position of the*I-th* nucleus and energy of the *i-th* orbital, respectively. Positions are computed by Equation (7) and energies of orbitals

Trial Version Wondershare PDFelement

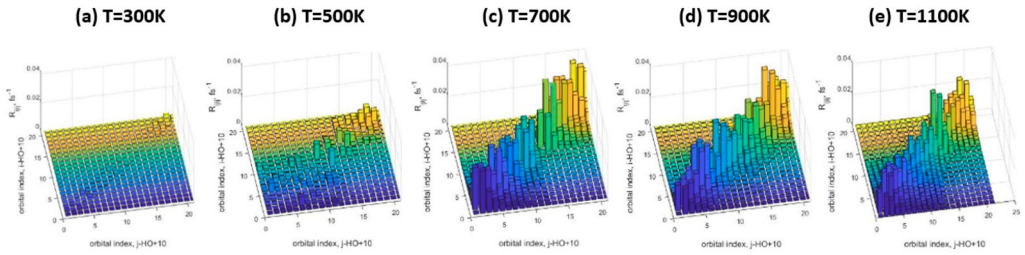


**Figure 7.** Redfield tensors at various temperatures. This figure shows the transition rates for pairs of orbitals in the range from HO-10 to LU+10. The rates undergo a substantial increase at 700 K. Subsequently, the rates appear to equalise along the main diagonal.

are computed by Equation (1). Note that upper-case Latin indices $I$ label nuclei and lower-case Latin indices $i$ label orbitals. In other words, the energies depend on the nucleus' position, which, in turn, depends on time. Figure S1 represents an example of Kohn–Sham energy fluctuations when the system was heated to 1100 K. Initially, the bandgap is approximately 1 eV at t = 0 femtoseconds. The interval from 0 fs to 150 fs in Figure S1 shows the dynamics when the model is on the way to approach thermal equilibrium. During this time interval, there is an interesting observation of the gap dynamically changing in time. As time progresses, the bandgap decreases until it eventually becomes zero. After $t > 150$ fs, the model is in the equilibrium and can be used for productive generation of non-adiabatic couplings. Note that at lower temperatures the gap remains open.

Figure 7 shows elements of Redfield tensors computed by Equations (9b)–(9d). Figure 7 shows that the rates of transitions between orbitals increase if we put system on a thermostat with larger temperature. One interpretation of this is as follows. At higher temperatures, the amplitude of fluctuations increases and orbitals gaps/sub-gaps temporarily close. This could be one of the underlying mechanisms increases the transition rate. Another underlying mechanism is that larger amplitude of nuclear motion gives larger violation of the orthogonality or pairs of orbitals. Note that temperature fluctuations, as shown in Figure S1, contribute to the enhancement of relaxation rates.

At lower temperatures, the transition rates near the bandgap are close to zero. Note that Figure 7 shows a positive correlation between the temperature and transition rate. This is expected. As temperature increases electrons will have more energy to jump between orbitals. Note that this is also due to a change in time. Furthermore, as temperature increases the gap between the conduction and valence band decreases. Another feature of interest is that at lower temperatures transitions between HOMO and LUMO have negligible transition rates compared to other pairs of orbitals. However, as temperature increases transition rates are more evenly distributed among pairs orbitals. States in middle contribute to PbTe → PbTe transitions, states in top right are PbTe → I transitions, and states in top left are PbTe→Na transitions.

Additionally, the orbitals furthest away from HOMO and LUMO have very high transition rates, as shown in Figure 7. This is consistent with Figure 1. At the start of the time step the bandgap is around 1 eV. However, as time goes on and temperature increases, the bandgap decreases and the transition rates for orbitals adjacent to HOMO and LUMO increase. There are two causes: the temperature increase and non-equilibrium dynamics. The second one is congruent with the differences in panels a and e of Figure 7. At 1100 K Figure 7(panel e), the values of transition rates among orbitals are quite homogeneous somewhat more in congruent than in Figure 7(panel a). However, at later temperatures these transition rates increase.

After computing the individual elements of the R-tensor, one is able to solve the equation of motion for density matrix at a range of different initial conditions. The initial conditions introduced in Equation (10c) are specified by a pair of orbitals ($HO\text{-}a$, $LU+b$) that have been driven away from equilibrium configuration. Here, we label initial excitation by the pairs of orbitals: first, an orbital $a$ that was occupied before the excitation event, that is typically an orbital in the valence band labelled as $HO\text{-}a$, and second, an orbital $b$ to where the electron has been promoted as a result of the initial excitation, the second orbital is typically in the conduction band and is labelled as $LU+b$. Solutions for each initial condition can be used for computing distributions, observables and their visual interpretation.

First, in Figure 8 charge density distribution is shown as a function of energy by using density matrix dynamics (which studied how density changed with time). They are computed according to Equation (11). Yellow and Blue colours correspond to excess $n(\varepsilon, t) > 0$ and deficiency $n(\varepsilon, t) < 0$ of electron at certain energy, at certain time. Green corresponds to equilibrium distribution $n(\varepsilon, t) = 0$. The expectation values of electron and hole energy

Trial Version Wondershare PDFelement

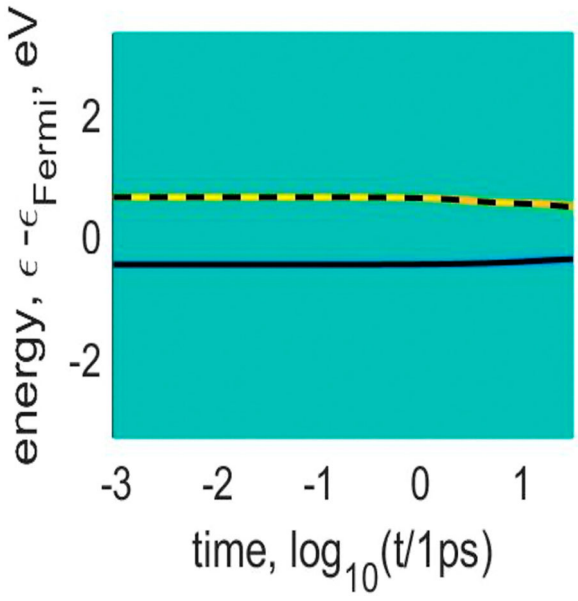


**Figure 8.** Representative dynamics of density distribution as function of energy $\Delta n(\varepsilon, t)$introduced in Equation (11) for initial excitation HO-4→LU+9, at T = 300K. Yellow and Blue colours correspond to excess $\Delta n > 0$ and deficiency $\Delta n < 0$ of electron at certain energies at certain times. Green corresponds to equilibrium distribution $\Delta n = 0$. Dashed and solid lines correspond to expectation values of energy of electron $\langle E_e \rangle$ (t)and hole $\langle E_h \rangle$ (t), as defined in Equation (12a)–(12b). At lower temperatures, the change in energy for both the electron and hole are relatively negligible compared to the dynamics computed for higher temperatures. Note that one can obtain relaxation rates for both electron and hole as time derivatives or integration of these expectation values, as defined in Equations (13)–(14). More info in Figure S2.

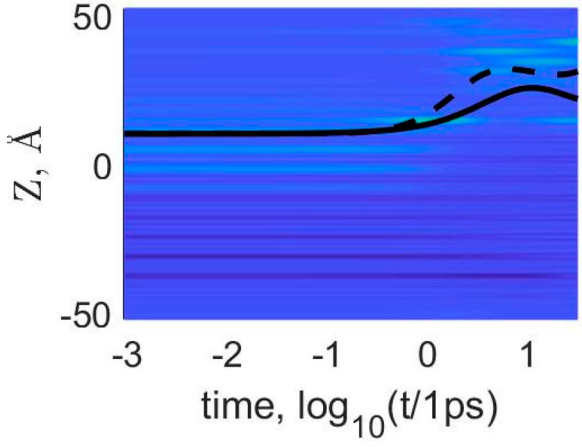


**Figure 9.** Dynamics of density distribution as a function of distance $\Delta n(z, t)$ defined by Equation (16c), for initial excitation (HO-4; LU+9), at T = 300K. Solid line = hole position computed by Equation (16d); Dashed line = electron position computed by Equation (16e). Yellow = excess of electron $\Delta n > 0$. Green = excess of hole $\Delta n < 0$. Blue = equilibrium $\Delta n = 0$. Solid and dashed lines start at the same point; as time passes bythey follow different trajectories: dashed tent to I, solid leans towards Na. More info in Figure S3. Note that all charge transfer is localised around the iodine dopants and that the transition rates increase with temperature.

were computed by Equations (12a) and (12b) and represented by dashed and solid line, respectively. More details are provided in Figure S2. Figure S2 shows that at lower temperatures the electron and hole relaxation rates were almost negligible. However, at higher values of temperatures relaxation occurs at earlier times. There is one expected trend from these figures. As the temperature increases, the energy difference between the electron and hole decreases.

In Figure 9, density distribution is studied in relation to the electron's position in space, computed with Equation (16). Colour codes math those fo Figure 8. Additional details are provided in Figure S3. As time passes by, the distance between average position of electron and hole increases. Two conclusions can be inferred from a qualitative examination of the graphs. First, all charge transfer is localised near the iodine dopants. This finding agrees with the chemical nature of iodine. Since iodine only needs one valence electron to complete its outer shell, it makes sense that an electron from the sodium dopant would travel toward the iodine dopant. Also, the electron appears to be travelling to the outermost iodine dopant.

Furthermore, according to Figure S3 the transition rate ($fs^{-1}$) increases with temperature until 700 K after which it plateaus. That is, the higher the temperature the quicker the electron's displacement between its initial and final points. This finding agrees with Figure 7. At lower temperatures, only outlier orbital pair transitions away from the HOMO and LUMO had the nonvanishing rates. However, as the temperature increases, all orbital pair transitions, including the ones near HOMO and LUMO, have nearly equal probability. The electron can travel quicker because it has a greater number of pathways available to it. Greater number of states implies more options for the electron to travel quicker.

Figure 10 reports rates computed by Equation (14) for different initial excitations of the model and at different temperatures. In Figure 10, a more quantitative examination is taken. Relaxation rates are studied as a function of excitation energy (related to the total amount of energy dissipated into heat during relaxation). A look at Figure 10(a) shows that the bandgap law ($K_{e/h} = Ae^{-\alpha \Delta E}$) appears to only apply to orbital transitions at higher temperatures. Also, there is negligible change of the relaxation rate with energy at the lower temperatures. Perhaps one reason for this is the decrease with the bandgap with respect to temperature. When the bandgap decreases at higher temperatures (this is corroborated by Figure S1), the 'energy' an electron needs to emit

Trial Version Wondershare PDFelement

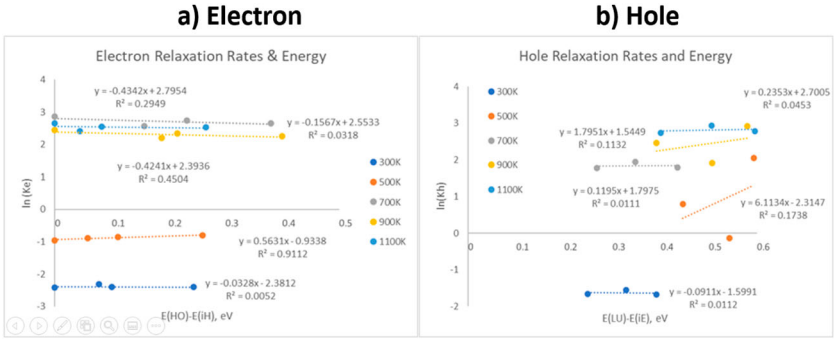


**Figure 10.** Relaxation rates $k_e$ (left panel) and $k_h$ (right panel) computed by Equation (14) as a function of Energy of initial excitation $\Delta E = \varepsilon_b - \varepsilon_{LU}$ for electrons and $\Delta E = \varepsilon_{HO} - \varepsilon_a$, where the pair of initially perturbed orbitals (a,b) determine initial condition. Relaxation rates for both the electron and hole are plotted in lo scale to check the agreement between computed data and expected trend of the bandgap law, defined in Equation (15). Results demonstrate moderate agreement for electron and little correlation for the hole.

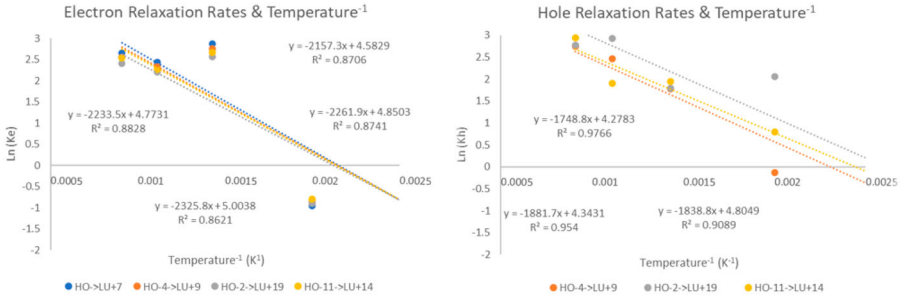


**Figure 11.** Relaxation rates $k_e$ (left panel) and $k_h$ (right panel) computed by Equation (14) as a function of inverse Temperature. Results show that the change of relaxation rates with respect to temperature is very similar regardless of initial orbital conditions. This demonstrates that the relaxation rates follow functional form of Arrhenius law originating form Boltzmann distribution.

decreases. As a result, it is easier for an electron to go down an orbital. Figure 10(b) shows limited correlation of the hole with the bandgap law.

Additionally, Figure 11 shows that the trends in the dependence of the electron and hole relaxation rates with temperature are independent of orbital pair transitions. A qualitative examination of these figures illustrates that these figures agree with the Arrhenius law and Boltzmnn distribution, where the relaxation rates have an exponential relation to temperature. Specifically, this proves that $\alpha = 1/k_B T$ where $T$ is the temperature and $k_B$ is the Boltzmann
constant.

## Discussion

This section contains interpretation and discussion on the use of certain exchange–correlation functionals: One scheme to accurately describe the bandgap is to perform calculations at the Heyd–Scuseria–Ernzerhof (HSE06) [45,46] hybrid functional level with the inclusion of SOC effect. The work by Stevanovich *et al.* [47] reports the following trend of matching the bandgap of un-doped lead telluride by using a range of functionals: PBE without spin–orbit correction gives moderate overestimation of the bandgap. Hybrid functional HSE06 without spin–orbit correction drastically overestimates bandgap. HSE06 with spin–orbit correction provides the bandgap closest to the experimental value, however, stays expensive for computation on non-adiabatic couplings. The adoption of PBE without SOC is still meaningful to follow qualitative trends. There are expectations that the use of the hybrid functional HSE06 with SOC corrections will keep the main trends observed in this work, while providing quantitative improvement, as it was recently done for other semiconductor nanostructures [48,49]. Discussion and validation for the use of PBE vs HSE06 exchange–correlation functionals for non-adiabatic couplings has been analysed in the literature, with the common opinion that the values of energies have sensitivity to the choice of functional, while shapes of orbitals and non-adiabatic couplings have less sensitivity to the choice of the functional [49,50].

This work reports case study of excited state dynamics of a candidate thermoelectric material. Based on the observed trends one may suggest future exploration of differences and similarities between approaches in

Trial Version Wondershare PDFelement

computational modelling of photovoltaic and thermoelectric effects.

## Conclusions

This first principle numerical experiment has yielded several interesting findings. One of such findings is that doping improves a lead telluride nanowire's ability for charge transfer. Specifically, replacing two lead and two telluride atoms with sodium and iodine, respectively, enables charge transfer. When contrasting results for a doped and un-doped model, one finds that co-doped lead telluride has a lower rate of absorbing photoenergy at the bandgap. Note that it could still be efficient above the gap. This, in turn, leads to fast phonon-induced non-radiative transitions between the conduction and valence bands.

The most important aspect of this study is how well the energy relaxation rates correlate with the energy gap law. Computations reveal two fashions of relaxation: sequential and parallel. Only sequential pathway of relaxation follows the energy gap law. The parallel pathway often violates gap law as there are more and more parallel channels available as one increases the excitation energy. This atomistic computational study shows that in the studied material/nanostructures, the energy gap law only applies to electrons at higher temperatures and shows less correlation with the trends in relaxation rates of holes. Furthermore, this study has shown that the general trend in the relaxation rates' dependence on temperature is independent of initial choice of excited orbitals/initial conditions.

However, in the future, one could be interested in analysing transitions starting from initial conditions represented by a superposition of orbitals to determine if the energy gap law still applies in that situation. This is important since real-world applications often have such type of initial photo- or thermal-excitation. Other future research direction is to contrast the findings of this numerical experiment with exploration of other models, such as doped and un-doped corresponding to a nanowire grown in $<111>$ direction. Relaxation rates, density of states, absorption spectra and other observables may need to be computed to compare with this study. Note that previous studies have shown that there is no momentum dispersion for $<111>$ nanowires. Furthermore, doping a helical nanowire is expected to affect its bandgap.

The findings, observations, and trends obtained in this atomistic computational modelling of photoinduced dynamics in certain classes of nanostructures have a potential of applicability to industry. First, this work provides a numerical proof of intuitively expected trend that doping facilitates charge transfer. Second, for a long time, researchers and producers have to undergo long and laborious studies to calculate relaxation rates for a material. However, if future studies corroborate the findings of this work and prove that the bandgap law has at least limited applicability, then the time for research and development in industry can be greatly reduced. Additionally, the greater the correlation between the relaxation rates and the bandgap law, the more efficient a thermoelectric material is. The authors would like to share curiosity and enthusiasm to the exploration of possible differences and similarities in the selection criteria of best materials for photovoltaic and thermoelectric applications.

## Acknowledgement

The authors thank DOE BES NERSC facility for computational resources, allocation award #91202, 'Computational Modeling of Photo-catalysis and Photo-induced Charge Transfer Dynamics on Surfaces' supported by the Office of Science of the DOE under contract no. DE-AC02-05CH11231. DSK acknowledges support of the National Science Foundation under grant numbers CHE-2004197 and CHE-1944921. The work of T.M.I. was performed under the state assignment of IGM SB RAS. KG acknowledges support of the Department of Physics, NDSU and the American Physical Society Bridge Program. The authors thank David Micha and Svetlana Kilina for inspiring ideas. They also thank Yulun Han, Fatima, Aaron Forde for discussions.

## Disclosure statement

No potential conflict of interest was reported by the author(s).

## Funding

The authors thank DOE BES NERSC facility for computational resources, allocation award #91202, 'Computational Modeling of Photo-catalysis and Photo-induced Charge Transfer Dynamics on Surfaces' supported by the Office of Science of the DOE under contract no. DE-AC02-05CH11231. DK acknowledges support of the National Science Foundation under grant number CHE-2004197. KG acknowledges support of the Department of Physics, NDSU and the American Physical Society Bridge programme; Division of Chemistry; National Science Foundation [grant number 1944921].

## ORCID

*Talgat M. Inerbaev* http://orcid.org/0000-0003-2378-4082
*D. S. Kilin* http://orcid.org/0000-0001-7847-5549

## References

[1] G.J. Snyder, Energy Environ. Sci. 10 (11), 2280–2283 (2017). doi:10.1039/C7EE02007D
[2] L.B. Kong. *Waste Energy Harvesting*. Lecture Notes in Energy, **24**. (Springer, Berlin, 2014), pp. 263–403.

Trial Version Wondershare PDFelement


[3] J.P. Heremans, V. Jovovic, E.S. Toberer, A. Saramat, K. Kurosaki, A. Charoenphakdee, S. Yamanaka and G.J. Snyder, Science. 321 (5888), 554–557 (2008). doi:10.1126/science.1159725

[4] Y. Pei, A. Lalonde, S. Iwanaga and G.J. Snyder, Energy Environ. Sci. 4 (6), 2085 (2011). doi:10.1039/c0ee00456a

[5] Y. Pei, X. Shi, A. Lalonde, H. Wang, L. Chen and G.J. Snyder, Nature. 473 (7345), 66–69 (2011). doi:10.1038/nature09996

[6] D. Quick, *World's Most Efficient Thermoelectric Material Developed. Gizmag* (2012).

[7] K. Biswas, J. He, I.D. Blum, C.I. Wu, T.P. Hogan, D.N. Seidman, V.P. Dravid and M.G. Kanatzidis, Nature. 489 (7416), 414–418 (2018). doi:10.1038/nature11439

[8] A.G. Redfield, IBM J. Res. Dev. 1 (1), 19–31 (1957). doi:10.1147/rd.11.0019

[9] A. Nitzan, *Chemical Dynamics in Condensed Phases: Relaxation, Transfer and Reactions in Condensed Molecular Systems* (OUP Oxford, New York, 2006).

[10] S.P. Webb, T. Iordanov and S. Hammes-Schiffer, J. Chem. Phys. 117 (9), 4106–4118 (2002). doi:10.1063/1.1494980

[11] S. Hammes-Schiffer, Abstracts of Papers of the American Chemical Society, 242 (2011).

[12] J.C. Tully, J. Chem. Phys. 93 (2), 1061–1071 (1990). doi:10.1063/1.459170

[13] S.V. Kilina, C.F. Craig, D.S. Kilin, O.V. Prezhdo, J. Phys. Chem. C. **111** (12), 4871–4878 (2007). doi:10.1021/jp0669052.

[14] S.V. Kilina, D.S. Kilin and O.V. Prezhdo, Acs Nano. 3 (1), 93–99 (2009). doi:10.1021/nn800674n

[15] S.V. Kilina, D.S. Kilin, V.V. Prezhdo, O.V. Prezhdo, J. Phys. Chem. C. **115** (44), 21641–21651 (2011). doi:10.1021/jp206594e

[16] S. Fernandez-Alberti, V.D. Kleiman, S. Tretiak, A.E. Roitberg, J. Phys. Chem. A. **113** (26), 7535–7542 (2009). doi:10.1021/jp900904q

[17] S. Fernandez-Alberti, V.D. Kleiman, S. Tretiak, A.E. Roitberg, J. Phys. Chem. Lett. **1** (18), 2699–2704 (2010). doi:10.1021/jz100794z

[18] T. Nelson, S. Fernandez-Alberti, V. Chernyak, A.E. Roitberg, and S. Tretiak, J. Phys. Chem. B. **115** (18), 5402–5414 (2011). doi:10.1021/jp109522g

[19] T. Nelson, S. Fernandez-Alberti, V. Chernyak, A.E. Roitberg, S. Tretiak, J. Chem. Phys. **136** (5), (2012). doi:10.1063/1.3680565

[20] L.G.C. Rego and V.S. Batista, J. Am. Chem. Soc. 125 (26), 7989–7997 (2003). doi:10.1021/ja0346330

[21] C.F. Craig, W.R. Duncan and O.V. Prezhdo, Phys. Rev. Lett. 95 (16), (2005). doi:10.1103/PhysRevLett.95.163001

[22] D.G. Tempel and A. Aspuru-Guzik, Chem. Phys. 391 (1), 130–142 (2011). doi:10.1016/j.chemphys.2011.03.014

[23] J.A. Parkhill, D.G. Tempel and A. Aspuru-Guzik, J. Chem. Phys. 136 (10), (2012). doi:10.1063/1.3689858

[24] D. Egorova, M. Thoss, W. Domcke, J. Chem. Phys. **119** (5), 2761–2773 (2003). doi:10.1063/1.1587121

[25] W.T. Pollard and R.A. Friesner, J. Chem. Phys. 100 (7), 5054–5065 (1994). doi:10.1063/1.467222

[26] W.T. Pollard, A.K. Felts and R.A. Friesner, Adv. Chem. Phys., Vol Xciii. 93, 77–134 (1996).

[27] J.M. Jean, R.A. Friesner and G.R. Fleming, J. Chem. Phys. 96 (8), 5827–5842 (1992). doi:10.1063/1.462858

[28] V. Sundstrom, T. Pullerits and R. van Grondelle, J. Phys. Chem. B. 103 (13), 2327–2346 (1999). doi:10.1021/jp983722+

[29] O. Kuhn, V. May and M. Schreiber, J. Chem. Phys. 101 (12), 10404–10415 (1994). doi:10.1063/1.467921

[30] W.B. Davis, M.R. Wasielewski, M.A. Ratner, V. Mujica, A. Nitzan, J. Phys. Chem. A. 101 (35), 6158–6164 (1997). doi:10.1021/jp970909c

[31] P.A. Apanasevich, S.Y. Kilin, A.P. Nizovtsev, N.S. Onishchenko, J. Opt. Soc. Am. B-Opt. Phys. **3** (4), 587–594 (1986). doi:10.1364/JOSAB.3.000587

[32] G. Kolesov and Y. Dahnovsky, Phys. Rev. B. 85 (24), 241309 (2012). doi:10.1103/PhysRevB.85.241309

[33] D.S. Kilin and D.A. Micha, J. Phys. Chem. Lett. 1 (7), 1073–1077 (2010). doi:10.1021/jz100122f

[34] J. Chen, A. Schmitz and D.S. Kilin, Int. J. Quantum Chem. 112, 3879 (2012). doi:10.1002/qua.24291

[35] P. Hohenberg and W. Kohn, Phys. Rev. 136 (3B), B864–B871 (1964). doi:10.1103/PhysRev.136.B864

[36] G. Kresse and J. Furthmüller, Phys. Rev. B. 54 (16), 11169–11186 (1996). doi:10.1103/PhysRevB.54.11169

[37] W. Kohn and L.J. Sham, Phys. Rev. 140 (4A), A1133–A1138 (1965). doi:10.1103/PhysRev.140.A1133

[38] J.P. Perdew, K. Burke and M. Ernzerhof, Phys. Rev. Lett. 77 (18), 3865–3868 (1996). doi:10.1103/PhysRevLett.77.3865

[39] J.P. Perdew, K. Burke, and M. Ernzerhof, Phys. Rev. Lett. 78 (7), 1396 (1997). doi:10.1103/PhysRevLett.78.1396

[40] J.M. Ziman, *Principles of the Theory of Solids* (Cambridge University Press, 1972). Chap. 7, pp. 211–254.

[41] D.S. Kilin and D.A. Micha, Chem. Phys. Lett. 461 (4–6), 266–270 (2008). doi:10.1016/j.cplett.2008.07.031

[42] D.S. Kilin and D.A. Micha, J. Phys. Chem. C. 113 (9), 3530–3542 (2009). doi:10.1021/jp808908x

[43] D.S. Kilin and D.A. Micha, J. Phys. Chem. C. 115 (3), 770–775 (2011). doi:10.1021/jp110756u

[44] C. Kittel, *Introduction to Solid State Physics*, 7th ed. (Wiley, New York, 1996; 197–232).

[45] J. Heyd, G.E. Scuseria and M. Ernzerhof, J. Chem. Phys. 118 (18), 8207–8215 (2003). doi:10.1063/1.1564060

[46] J. Heyd, G.E. Scuseria, and M. Ernzerhof, J. Chem. Phys. **124** (21), 219906 (2006). doi:10.1063/1.2204597

[47] A. Goyal, P. Gorai, E.S. Toberer and V. Stevanović, npj Comput. Mater. 3 (1), 42 (2017). doi:10.1038/s41524-017-0047-6

[48] A. Forde, T. Inerbaev, E.K. Hobbie and D.S. Kilin, J. Am. Chem. Soc. 141 (10), 4388–4397 (2019). doi:10.1021/jacs.8b13385

[49] Y. Han and D.S. Kilin, J. Phys. Chem. Lett. 11 (23), 9983–9989 (2020). doi:10.1021/acs.jpclett.0c02973

[50] N. Voudoukis, Eur. J. Electr. Eng. Comput. Sci. 2 (1), (2018). doi:10.24018/ejece.2018.2.1.13